Open Research Online

The Open University's repository of research publications
and other research outputs

Dynamics of Fattening and Thinning 2D Sessile Droplets

Journal Item

For guidance on citations see FAQs.

oro.open.ac.uk

The dynamics of fattening and thinning 2D sessile droplets

M. Pradas,[*,†] N. Savva,[‡] J. B. Benziger,[¶] I. G. Kevrekidis,[¶,§,‖] and S. Kalliadasis[⊥]

†*Department of Mathematics and Statistics, The Open University, Walton Hall, Milton Keynes, MK7 6AA, United Kingdom*

‡*School of Mathematics, Cardiff University, Cardiff CF24 4AG, United Kingdom*

¶*Department of Chemical and Biological Engineering, Princeton University, Princeton, New Jersey 08544, United States*

§*Program in Applied and Computational Mathematics, Princeton University, Princeton, New Jersey 08544, United States*

‖*TUM-Institute for Advanced Study, Lichtenbergstrasse 2 a, 85748 Garching, Germany*

⊥*Department of Chemical Engineering, Imperial College London, London SW7 2AZ, United Kingdom*

E-mail: marc.pradas@open.ac.uk

Abstract

We investigate the dynamics of a droplet on a planar substrate as the droplet volume changes dynamically due to liquid being pumped in or out through a pore. We adopt a diffuse-interface formulation which is appropriately modified to account for a localized inflow-outflow boundary condition (the pore) at the bottom of the droplet, hence allowing to dynamically control its volume, as the droplet moves on a flat substrate with a periodic chemical pattern. We find that the droplet undergoes a stick-slip

motion as the volume is increased (fattening droplet) which can be monitored by track-
ing the droplet contact points. If we then switch over to outflow conditions (thinning
droplet) the droplet follows a different path (i.e. the distance of the droplet midpoint
from the pore location evolves differently) giving rise to a hysteretic behavior. By
means of geometrical arguments we are able to theoretically construct the full bifur-
cation diagram of the droplet equilibria (positions and droplet shapes) as the droplet
volume is changed, finding excellent agreement with time-dependent computations of
our diffuse-interface model.

Introduction

Droplet spreading and associated wetting phenomena are ubiquitous in a wide spectrum
of natural systems and technological applications, from the way rain droplets interact with
plant leaves and insects walking on water, to microchemical reactors, fluid transport pro-
cesses, materials processing and the rapidly growing field of micro- and nanofluidics, to
name but a few. In most cases, the substrates on which droplets spread are not smooth but
are characterized by various complexities such as chemical and/or topographical variations-
heterogeneities which can give rise to very rich dynamics characterized by, e.g., hysteresis
behavior and stick-slip motion.[1–11] Examples of complex substrates also include the case
of a membrane or a porous medium, where, in addition to the intrinsic properties of the
material, one needs to take into account the fact that the volume of the droplet may vary in
time. In particular, an important feature here is that liquid can be absorbed or pumped in
through the membrane,[12,13] i.e. the droplet may be fattening or thinning, something common
in e.g. polymer electrolyte membrane (PEM) fuel cells.[14–17]

In such cells, water is formed at a catalyst/membrane interface and is pushed through
porous electrodes into the gas flow channel. It has been observed (and explained through
the hydrophobicity of the porous material of the electrodes) that water droplets emerge from
the *largest* pores in the electrode gas diffusion layer (GDL) and grow in the main channel,

2

i.e. droplets experience a dynamic volume variation.[16] The droplets will then detach and be pushed by the gas flowing through the channel while remaining in contact with the GDL porous surface. Ultimately, they need to be removed from the device to avoid issues such as flooding. Once the droplets are created and grow into the main channel, they are constantly in contact with a disordered substrate (i.e. the electrode GDL) which may affect the whole process.

In addition to PEM fuel cells, droplets with time-dependent volume are found in many other applications and natural systems, such as for example microemulsification, problems with non-equilibrium thermal effects, such as evaporation and condensation,[7,18–24] and chaotic behaviour such as drops in a dripping faucet,[25,26] but also natural systems such as droplet growth in speleothem drip sites.[27] In addition to its significance in numerous applications in nature and technology, understanding the interplay between dynamic volume variation and other parameters, e.g. the substrate chemical properties and geometry, is one of the basic questions that must be addressed from the fundamental fluid dynamics point of view.

Here we investigate a simple prototype system, a two-dimensional (2D) droplet sitting on a horizontal substrate with a small pore from which liquid can be pumped in or out of the droplet; we have already referred to it as a fattening or thinning droplet, respectively. To this end, we adopt a diffuse-interface Cahn-Hilliard model (see e.g. Refs. 8) that incorporates an extra boundary condition (BC) which allows us to impose either a positive (inflow) or negative (outflow) constant liquid flux into the droplet at a pore, hence allowing us to dynamically control its volume. As far as the solid substrate is concerned, we consider a topographically smooth substrate but with a chemical heterogeneity that consists of a spatially periodic chemical pattern, i.e. the local equilibrium contact angle varies periodically along the substrate.

The problem of dynamic droplet volume variation has received some attention over the last few decades, both experimentally[28–30] and analytically-computationally,[31–34] however, it

is still unclear how the dynamics of the droplet itself, as its volume increases or decreases in time, is affected by the properties of the solid substrate. As far as the influence of chemically heterogeneous substrates is concerned, we note the study in Ref. 32 of a 2D droplet on a horizontal chemical heterogeneous substrate, but without inflow-outflow as we do here, and where bifurcation diagrams for the droplet half-width/radius and contact angle as a function of volume were given, pointing also to the possibility of contact angle hysteresis. However, the volume was not changed *dynamically* as in our study; instead it was considered as a varying parameter in an equation governing droplet equilibrium, and as such Ref. 32 was restricted to equilibrium only. Moreover, the analysis in Ref. 32 considered only the case in which the droplet is kept fixed at a specific point on the surface, hence not allowing for any possible horizontal motion of the droplet. In this sense, the bifurcation diagram we present here is more complete as we explore all the relevant variables of the problem.

We revisit the bifurcation diagram presented in Ref. 32 and perform a detailed and systematic parametric study of the slow dynamics of the droplet. It is important to note that under these conditions, the droplet never detaches from the pore. By making use of elements from dynamical systems theory we fully rationalize all bifurcations and the stability of the different solution branches as the volume dynamically varies. We argue that, in addition to the droplet volume which is the bifurcation parameter, the other pertinent variables are the droplet shift, a measure of the distance the droplet midpoint is displaced with respect to a reference point along the substrate, and the droplet half-width, a measure of the droplet radius, so that the bifurcation diagrams for the equilibrium solutions are in fact three dimensional (3D).

We demonstrate that the droplet exhibits stick-slip dynamics as the volume is increased (inflow conditions) which we monitor by recording the droplet shift. When we switch over to outflow conditions, i.e. the volume decreases, the droplet exhibits again stick-slip motion but it now follows a different path giving rise to hysteresis behavior. Hence, a simple prototypical chemically heterogeneous substrate can induce complex droplet dynamics.
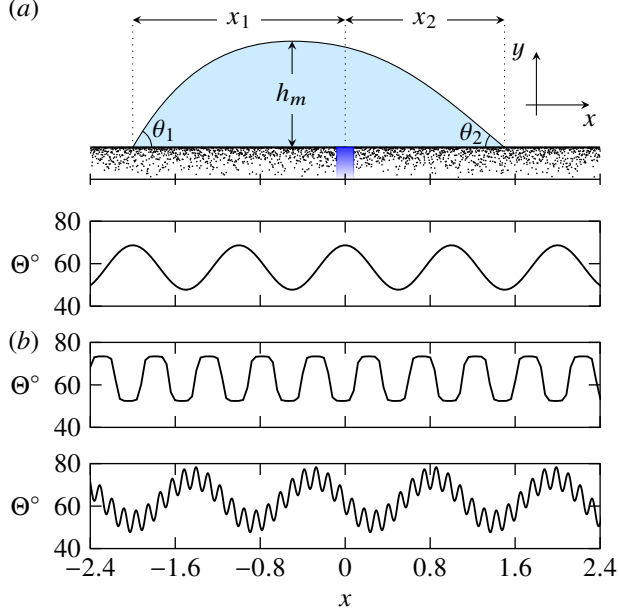
4

Figure 1: (a) Problem setup: a 2D droplet lies on a topographically flat but chemically heterogeneous substrate with the chemical heterogeneity described by the function $\Theta(x)$ (bottom panel). An inflow-outflow BC is imposed near the origin of the system and it is depicted as a blue patch. The position of the gas-liquid interface corresponds to a dynamic snapshot obtained with the diffuse-interface formulation described in the text. (b) Alternative types of periodic chemical heterogeneities considered in this study.

Problem formulation and theoretical framework

Our setup consists of a 2D droplet moving on a flat substrate which has been chemically altered so that its wetting properties vary periodically along the substrate. Hence, the equilibrium contact angle, which is defined as the angle between the liquid-gas interface and the wetted area of the substrate, is taken to vary periodically along the substrate. In the simplest case the equilibrium contact angle is prescribed by the spatially oscillatory function:

$$\Theta(x) = \theta_0 + \sigma \cos(2\pi x/\lambda), \tag{1}$$

where θ_0 is the equilibrium contact angle for the homogeneous substrate, and σ and λ represent the intensity and wavelength of the disorder variation, respectively. We are interested in studying the dynamic properties of the droplet as its volume is increased (fattening droplet)

5

or decreased (thinning droplet) and so we impose a BC on the substrate through which liquid can be pumped in or out of the droplet.

Let x_1 and x_2 denote the position of the left and right contact points of the droplet, respectively, and $h(x,t)$ the liquid-gas interface position. To interrogate the droplet dynamics we then monitor different dynamic quantities describing the droplet as the volume $V(t) = \int_{x_1}^{x_2} h(x,t)dx$ varies in time, namely the droplet shift, $\ell = [x_1(t) + x_2(t)]/2$, which measures the distance the droplet midpoint is displaced from $x = 0$, the droplet half-width, $d(t) = [x_2(t) - x_1(t)]/2$, measuring the droplet radius and the contact angles $\theta_1(t)$ and $\theta_2(t)$, corresponding to the left and right contact points, respectively. Figure 1(a) shows a computational result, obtained with the methodology described below together with the definition of all relevant quantities, and Figure 1(b) shows two additional examples of periodic chemical heterogeneities considered in this work, namely a striped version of eq 1,

$$\Theta(x) = \theta_0 + \sigma \tanh\left[\lambda_t \cos\left(2\pi x/\lambda\right)\right], \tag{2}$$

where λ_t is an additional parameter controlling the steepness of the chemical variation, and a multiscale version of eq 1 (bottom panel):

$$\Theta(x) = \theta_0 + \sigma \sin\left(2\pi x/\lambda\right) + \sigma_2 \sin\left[2\pi x/(\epsilon\lambda)\right], \tag{3}$$

where $\epsilon \ll 1$ is a small parameter.

Equilibrium properties

In the absence of any overhead gas flow and for a constant volume $V = \int_{x_1}^{x_2} h_0(x)\mathrm{d}x$, we have that, at equilibrium, the contact angles for a 2D system need be equal to each other,[35] i.e. $\theta_1 = \theta_2 = \theta$.

In addition, in the absence of gravity the free surface is given by a circular arc which is uniquely determined by the contact angle θ and the droplet half-width d. Under these
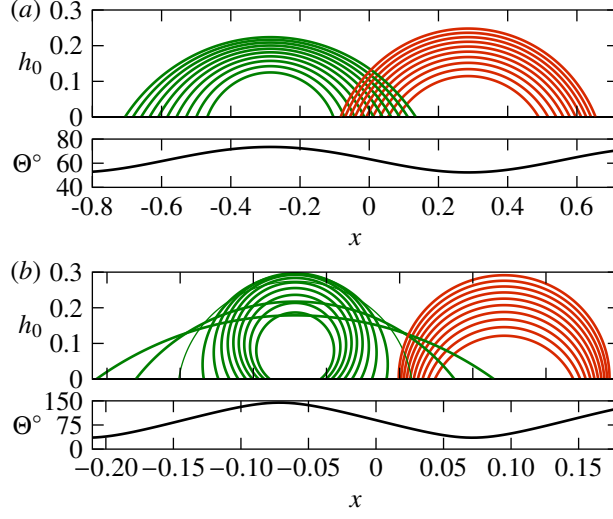
Figure 2: Equilibrium droplet profiles obtained from eqs 4 and 5 for different values of V for a chemical heterogeneity given by $\Theta(x) = \theta_0 + \sigma \sin(2\pi x/\lambda)$ with: (a) $\theta_0 = 59°$, $\lambda = 1.2$, and $\sigma = 11$; and (b) $\theta_0 = 90°$, $\lambda = 0.3$, and $\sigma = 60$.

assumptions, we have the following relation:[32]

$$V = \frac{d^2}{2} \frac{2\theta - \sin(2\theta)}{\sin^2 \theta}. \tag{4}$$

Since the contact angle at each point of the substrate is given by the function $\Theta(x)$, for a given droplet shift ℓ, we have that the following two conditions must also hold at equilibrium:

$$\theta(d; V) - \Theta(\ell + d) = 0, \tag{5a}$$

$$\theta(d; V) - \Theta(\ell - d) = 0, \tag{5b}$$

where $\theta(d; V)$ is determined from eq 4. Thus, the equilibrium solutions at any volume are found by solving the above system of equations for d and ℓ numerically. Figure 2 depicts an example of different equilibrium profiles found for different values of V and for two different sets of parameters in the chemical heterogeneity, namely a hydrophilic substrate with an average contact angle of $\theta_0 = 59°$ (Figure 2a), and an alternating hydrophilic and
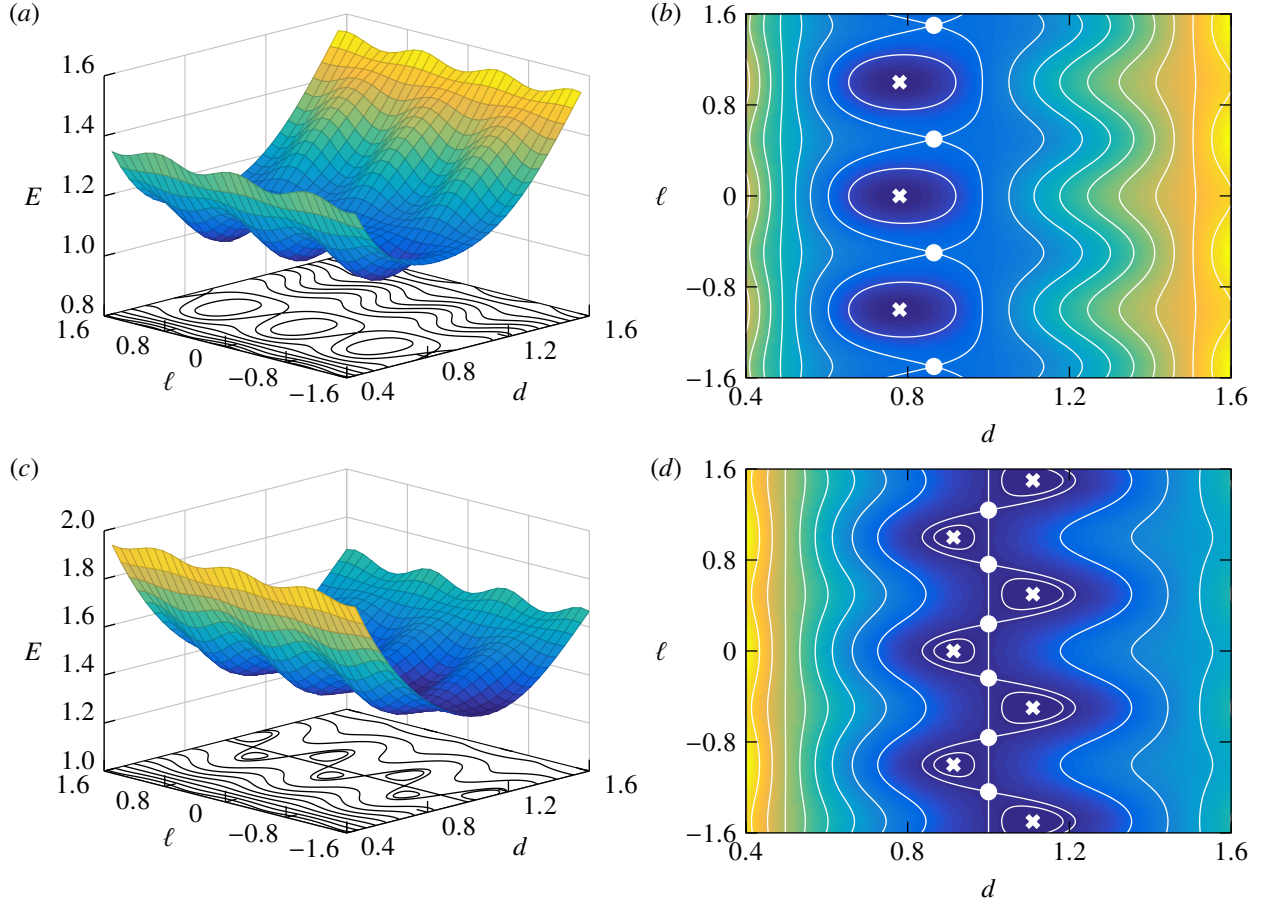
7

Figure 3: Energy landscapes for the chemical heterogeneity given by eq 1 with $\theta_0 = 58°$, $\lambda = 1$, and $\sigma = 10$; and for two different volumes, $V = 0.5$ (a,b) and $V = 0.8$ (c,d). The right panels show the corresponding contour plots where crosses and solid circles represent the position of stable and saddle nodes, respectively. The color shading is from yellow (high energy) to dark blue (low energy).

hydrophobic substrate with an average contact angle of $\theta_0 = 90°$ (Figure 2b).

Energy of the system

Alternatively, we can also find the equilibrium points and their stability by looking at the

surface energy of the system[35] which for a 2D droplet of equal contact angles is given, in

dimensionless form, as:

$$E(\ell, d) = \frac{2\theta d}{\sin \theta} - \int_{\ell-d}^{\ell+d} \cos \Theta(x) \mathrm{d}x, \tag{6}$$

8

where we have considered a sufficiently small pore so that its effect on the surface energy is negligible. Clearly the system equilibria correspond to stationary points/extrema of the above energy function, i.e. when we have $\partial_\ell E(\ell, d) = \partial_d E(\ell, d) = 0$. Figure 3 depicts two energy landscapes corresponding to two different droplet volumes and for a sinusoidal chemical heterogeneity, with the location of the stable equilibria marked as crosses and the unstable saddle equilibria as solid cicles. By comparing Figures 3a and 3b, it is evident that changing the volume can largely modify the energy landscape of the system hence affecting the dynamics of the droplet.

Computational method: Diffuse interface formulation

To dynamically model our system we adopt a Cahn-Hilliard phase-field formulation which is generally used to describe a system of two phases separated by a diffuse interface (see e.g. Refs. 36–39). In this approach, a locally conserved field, denoted as ϕ, plays the role of an order parameter by taking two equilibrium limiting values $+\phi_e$ and $-\phi_e$ that represent the liquid and air phases, respectively. The interface position of the droplet, which we denote as $h(x, t)$, is then located at the points where the order parameter vanishes, i.e., for a 2D system we have $\phi[x, h(x, t)] = 0$. The equilibrium properties of the model are based on a Ginzburg-Landau formulation, where the total free energy of the system is given by

$$\mathfrak{F}[\phi] = \int_\Omega \mathrm{d}\mathbf{r} f(\phi) = \int_\Omega \mathrm{d}\mathbf{r} \left[V(\phi) + \frac{\varepsilon^2}{2} |\boldsymbol{\nabla}\phi|^2 \right], \tag{7}$$

where $f(\phi)$ is the free energy density, Ω corresponds to the whole domain of the liquid/air system, and the potential $V(\phi)$ is chosen as:

$$V(\phi) = -\frac{1}{2}\alpha\phi^2 + \frac{1}{4}\beta\phi^4, \tag{8}$$

9

with α and β being positive constants so that the equilibrium value for the phase field is given by $\phi_e = \sqrt{\alpha/\beta}$. The double-well form of the potential combined with the square gradient term of the free energy ensures the existence of a well-defined interface of width $\zeta = \varepsilon/\sqrt{\alpha}$. In this formulation, the chemical potential is defined as $\mu = \delta\mathfrak{F}/\delta\phi = V'(\phi) - \varepsilon^2 \nabla^2 \phi$, and the surface tension of the liquid-gas interface γ_{lg} can be easily obtained as the excess free energy per unit surface area due to the inhomogeneity in ϕ, which gives $\gamma_{\ell g} = \frac{2\sqrt{2}}{3}\zeta\alpha\phi_e^2$.[8,40]

To take into account the wetting properties of the solid substrate, the free-energy equation (7) is modified by adding an extra term associated with solid-fluid interactions[41]

$$\mathfrak{F}[\phi] = \int_\Omega d\mathbf{r} \left[V(\phi) + \frac{\varepsilon^2}{2}|\boldsymbol{\nabla}\phi|^2 \right] + \int_s d\mathbf{s} f_s(\phi_s), \tag{9}$$

where s denotes the solid surface. The function $f_s(\phi_s)$ in this additional term enables us to introduce wetting effects into the model. It is related to the molecular interactions between fluid and solid, and it is usually expanded as a power series in ϕ_s,[42] where ϕ_s represents the value of the phase field at the solid substrate. In the present study we shall keep only the first-order term and write: $f_s = -a\phi_s$, where a describes the preference of the wall for either the liquid phase ($a > 0$, hydrophilic conditions) or the air phase ($a < 0$, hydrophobic conditions). It is important to emphasize that the linear term in the expansion of f_s turns out to be sufficient to describe partial wetting situations[40,43] as the ones we are going to consider here. We note, however, that for settings close to complete wetting (i.e. contact angles close to zero) the inclusion of higher-order terms may be necessary to avoid effects induced by density gradients on the solid substrate due to, e.g., the formation of mesoscopic layers there.[44,45]

Our system is non-dimensionalized by choosing the following dimensionless variables:

$$\phi^* = \phi/\phi_e, \qquad \mathbf{r}^* = \mathbf{r}/\lambda, \tag{10a}$$

$$f^* = f/(\phi_e^2\alpha), \qquad f_s^* = f_s/\gamma_{\ell g}, \tag{10b}$$

where λ is the wavelength of the chemical heterogeneity. By minimizing the corresponding dimensionless free energy functional in eq 9, the equilibrium conditions are given by $\mu = \delta\mathfrak{F}/\delta\phi = 0$, corresponding to setting the chemical potential to zero, and the wetting boundary condition:[40,41]

$$\mathbf{n_y} \cdot \boldsymbol{\nabla}\phi|_s = \frac{\tilde{\gamma}}{C_n}\frac{\mathrm{d}f_s}{\mathrm{d}\phi_s} = -\frac{\tilde{\gamma}}{C_n}a, \tag{11}$$

where the asterisks have been dropped and we have defined the Cahn number as $C_n = \zeta/\lambda$, and $\tilde{\gamma} = 2\sqrt{2}\phi_e/3\gamma_{\ell g}$. Here, $\mathbf{n_y}$ is the normal outward unit vector to the substrate. For a constant value of a, the corresponding equilibrium contact angle, θ_e, can be obtained by making use of the Young-Dupré relation, $\cos\theta_e = (\gamma_{gs} - \gamma_{\ell s})/\gamma_{\ell g}$, giving rise to the following relation:[40,41,46,47]

$$\cos\theta_e = \frac{1}{2}\left[(1 + A)^{3/2} - (1 - A)^{3/2}\right], \tag{12}$$

where we have defined $A = \sqrt{2}\tilde{\gamma}a$. In this approach, the different surface tensions γ_{sg} and γ_{sl} can be obtained by integrating the free energy per unit area along the corresponding interfaces, solid-gas and solid-liquid.[40]

Finally, the dynamics of the phase field is assumed to follow a conservation equation, based on a time-dependent Ginzburg-Landau Hamiltonian (model B in the Hohenberg and Halperin nomenclature[48]). In dimensional form it reads:

$$\frac{\partial\phi}{\partial t} = \boldsymbol{\nabla} \cdot M\boldsymbol{\nabla}\mu = \boldsymbol{\nabla} \cdot M\boldsymbol{\nabla}\left(-\alpha\phi + \beta\phi^3 - \varepsilon^2\nabla^2\phi\right), \tag{13}$$

by using the diffusion time scale $\zeta^2/M\alpha$ as the characteristic time scale and where μ is the chemical potential defined earlier, and M is a mobility parameter, which in general depends on ϕ but for simplicity here we take $M = 1$. Strictly speaking, eq 13 (model B) is expected to be valid in a regime where the dynamics is dominated by diffusion-like mechanisms. In fact, as it was shown in the Appendix of Ref. 8, eq 13 can be obtained from the full equations for the order parameter ϕ (an advection-diffusion equation for ϕ that involves the velocity field, coupled to the Navier-Stokes equation for the velocity field) in the limit of small Péclet

number, in which diffusion dominates advection.

To implement an inflow-outflow BC with a single pore of length ℓ_p which is located within the region the droplet is lying on, we impose a constant gradient of chemical potential along ℓ_p. In particular, we take

$$\mathbf{n_y} \cdot \boldsymbol{\nabla}\mu|_{\{x \in [-\ell_p/2, +\ell_p/2], y=0\}} = -v_m, \tag{14}$$

where v_m is a constant parameter that controls the flow that is being pumped in $(v_m > 0)$ or out $(v_m < 0)$. In our numerical computations we fix the value $|v_m| = 0.01$ which guarantees a sufficiently slow dynamics.

The dimensionless form of eq 13 is numerically solved by making use of an explicit fourth-order Runge-Kutta algorithm with adaptive time stepsize, and a rectangular spatial discretization with grid $\Delta x = \Delta y = 0.05$. All numerical integrations presented in this study have been performed by setting the Cahn number to $C_n = 0.05$, and a fixed value of the pore length $\ell_p = 2\Delta x$. The interface position, $h(x,t)$, is estimated by a linear interpolation of the zero of the phase field, $\phi[x, h(x,t); t] = 0$. This allows us to estimate the position of the contact point of the liquid-air interface at the wall surface by using a parabolic extrapolation of the nearest points of the droplet (see Ref. 8 for more details).

Results

We start by considering the periodic chemical heterogeneity shown in the bottom panel in Figure 1a. In particular we assume that A in eq 12 varies as $A = 0.3 + \sigma_0 \cos(\lambda_0 x)$ with $\sigma_0 = 0.1$ and consider different values of λ_0. It can be shown that for this choice of A, the corresponding equilibrium contact angle (cf. eq 12) is well approximated by eq 1 with $\sigma = 10$, $\lambda = \lambda_0$, and $\theta_0 = 58°$. In our computations we take different ranges of the ratio between the droplet volume and the heterogeneity wavelength, which we quantify by the dimensionless parameter $\Lambda = d_0/\lambda$, where d_0 is the initial droplet radius. In addition, we impose an inflow
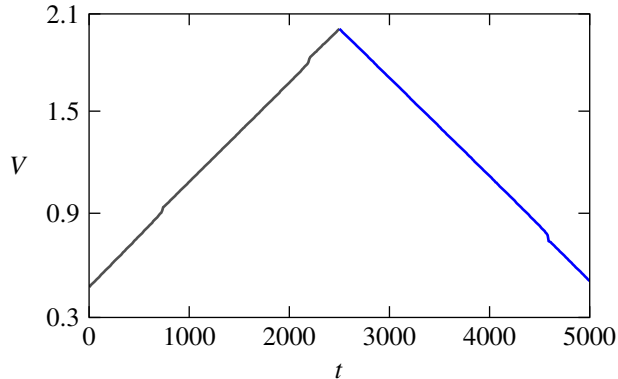
Figure 4: Time-dependent volume for inflow conditions (up to $t = t_f = 2500$, black line) and outflow conditions (for $t > t_f$, blue line).

BC until time t_f after which the BC is switched over to outflow conditions. Figure 4 shows the time-dependent variation of the volume which illustrates its linear evolution.

First, we perform a test of the stability of the equilibrium points of the system for a given volume by considering dynamic computations with initial conditions (ICs) generated from perturbed stable equilibrium profiles. The results are presented in Figure 5 demarcating the three different sets of computations with curves of different thickness. It is evident that any IC which is close to a stable equilibrium point will converge to that state for sufficiently long times. The middle panel of Figure 5 shows the corresponding path followed by the droplet projected onto the surface energy on the (d, ℓ) plane, demonstrating that the droplet is indeed moving towards the local minimum. For one set of computations (thinnest curves), the trajectory is initially attracted towards a saddle equilibrium, but then abruptly bends towards the stable equilibrium. This kind of behaviour typically manifests itself as stick-slip dynamics (see Ref. 35). We note that in all cases the solution adopts a circular arc for most of the time, except during the initial stage, which is a consequence of the imposed perturbed IC, and when the droplet exhibits stick-slip motion, which is when the two contact angles are different from each other. For example, we have measured the relative difference between the theoretically predicted energy E (given by eq 6) and the numerically computed energy E_n (obtained by integrating the interfacial energy of the droplet), and observed that $\Delta E \equiv |E - E_n|/E$ exhibits an increased peak from $\Delta E \sim 0.01$ up to $\Delta E \sim 0.04$ (note that
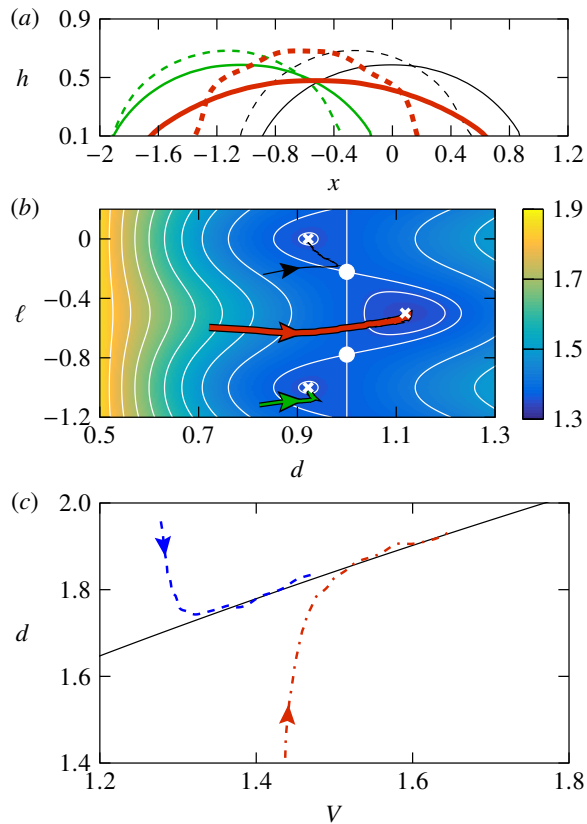
13

Figure 5: (a) Different ICs (dashed lines) which are sufficiently close to the equilibrium state converge to the equilibrium state (solid lines) at sufficiently long times. The three different sets of computations are distinguished from each other with curves of different thickness. Middle panel (b) shows the path of the droplet projected onto the (d, ℓ) plane with the surface energy landscape shaded according to the color bar on the right, where crosses and solid circles represent the position of stable and saddle nodes, respectively. (c) Evolution of the radius d as function of the volume V for two set of computations with homogeneous chemical properties and inflow conditions (dashed and dot-dashed lines). Solid line shows the analytical solution eq 4. In all panels, arrows indicate direction of time.

this is not shown in Figure 5) during the stick-slip motion observed in the set of computations whith the thinnest curves, indicating hence a deviation from the circular arc solution.

In addition, we perform a set of computations by considering a homogeneous chemical susbtrate and with a slow variation in the volume (inflow conditions). We consider two different ICs with a contact angle that is far from the equilibrium one. The bottom panel of Figure 5 shows the radius d as function of the volume V for both ICs, where we observe that the initial states relax to the corresponding value of d which is given by the analytical
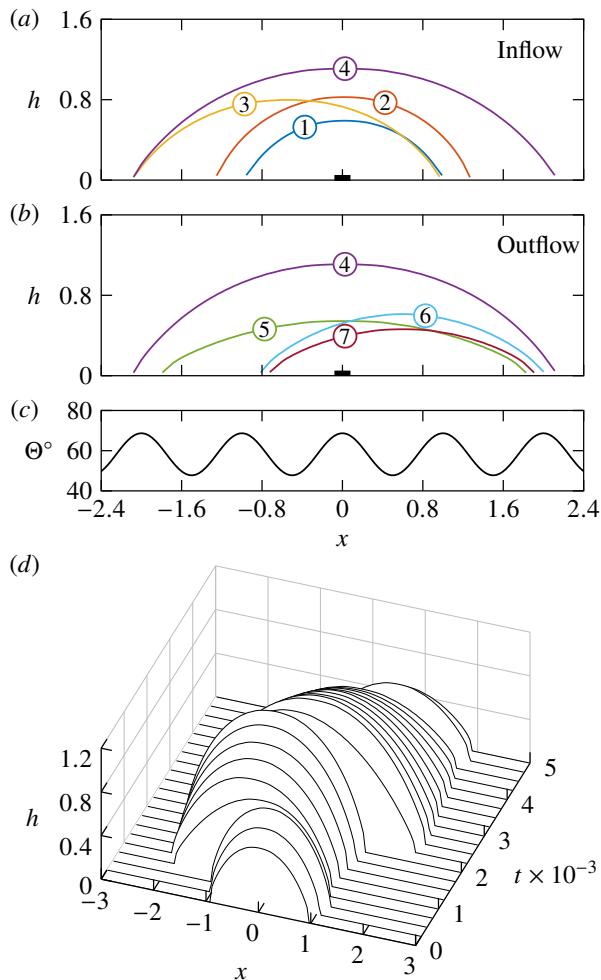
14

Figure 6: Droplet profiles for inflow, (a), and outflow conditions, (b) at different times. Profiles labelled 1 through 7 correspond to $t = 100, 700, 1000, 2500, 4500, 4650$ and 5000, respectively. At $t = 2500$ we switch from inflow to outflow BC (applied over the region demarcated by the thick line at $y = 0$) (c) Heterogeneity profile used for the results. (d) Spatio-temporal representation of the droplet dynamics during the inflow/outflow cycle.

solution eq 4 (solid line, note that the range used for V is quite short and hence the algebraic behaviour of eq 4 is not elucidated). This demonstrates that the Young-Dupré equation can be thought of as the "slow manifold" of the full diffuse-interface model.

Figure 6 shows snapshots of the dynamics of the droplet as the volume varies in time. When the volume increases, the droplet remains centered at the same position (i.e. the shift ℓ is not changing) until it reaches some critical volume for which the droplet suddenly shifts to the left (profile 3). As we keep increasing the volume, the droplet remains at this position
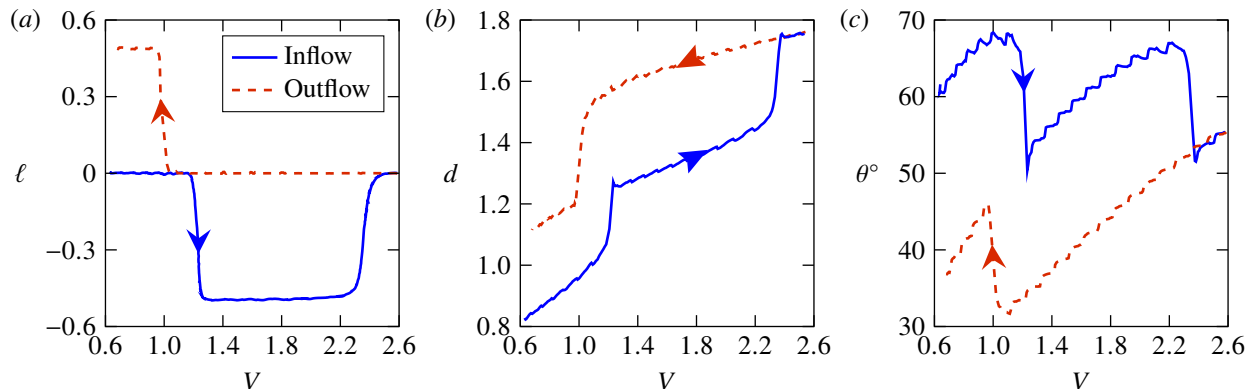
15

Figure 7: Computations of the different quantities characterizing the droplet dynamics as the volume is increased (blue solid lines) and decreased (red dashed lines) with a chemical heterogeneity given by eq 1 with $\Lambda = d_0/\lambda = 0.8$. (a) Shift ℓ, (b) droplet half-width d, and (c) one of the contact angles θ. In all panels, arrows indicate the direction of time.

for some range of volumes until it unpins, shifting to the right, thus becoming centred about $x = 0$ (profile 4). During this movement, one of the two contact points exhibits a stick-slip motion while the other one remains fixed nearly at the same position. At this point, we restart the computations with an outflow BC and the droplet volume decreases with its midpoint remaining fixed (cf. Figure 6b, profile 5). Below a critical volume the droplet shifts to the right and remains there as the volume keeps decreasing further (profiles 6 to 7).
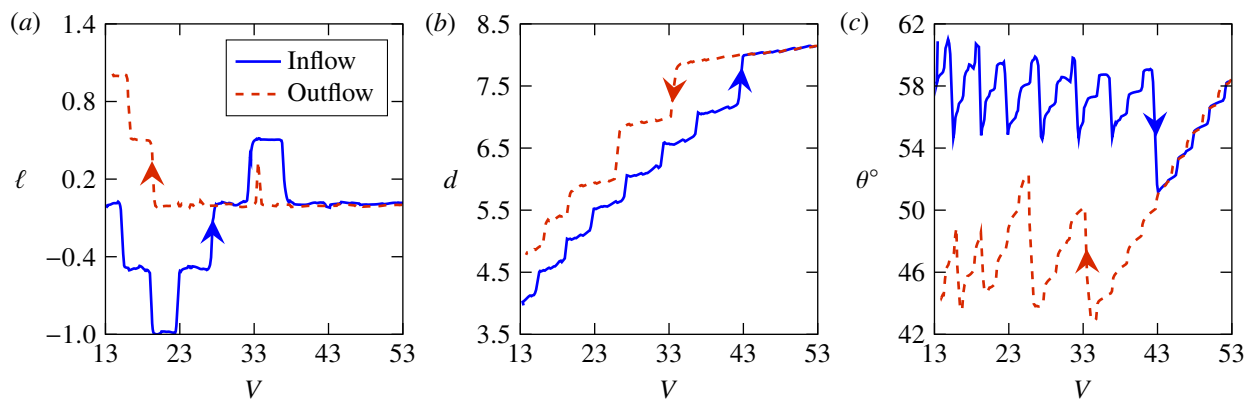

Figure 8: Computations of the different quantities characterizing the droplet dynamics as the volume is increased (blue solid lines) and decreased (red dashed lines) with a chemical heterogeneity given by eq 1 with $\Lambda = d_0/\lambda = 4$. (a) Shift ℓ, (b) droplet half-width d, and (c) one of the contact angles θ. In all panels, arrows indicate the direction of time.

To quantify the droplet dynamics, we monitor the droplet shift ℓ, the half-width d and

16

one of the contact angles, namely $\theta = \theta_1$. Figure 7 shows the evolution of all three quantities for the case of $\Lambda = 0.8$. We observe that the shift ℓ exhibits clear hysteresis as the volume is increased and decreased, a loop induced by the chemical heterogeneity. The droplet half-width and the contact angle exhibit a similar behavior characterized by stick-slip motion and hysteresis (we note that θ_2 would follow a similar trend with the only difference being during the rapid stick-slip movements which would occur at slightly different times). Interestingly, if we increase the value of Λ, which means that we either increase the initial volume of the droplet or alternatively decrease the wavelength of the chemical heterogeneity, such stick-slip motion becomes more prominent as the volume is increased/decreased. Figure 8 shows the numerical results with $\Lambda = 4$ where we can see that this is indeed the case. Consequently, the paths followed by a fattening and a thinning droplet appear to be markedly different, particularly for the shift ℓ (cf. Figure 8a).

In fact, we observe that as we keep repeating the process of increasing and decreasing the volume, the droplet settles into a dynamic behavior which is characterized by two distinct regimes. Figure 9a shows the shift of the droplet for two cycles of the inflow-outflow process with $\Lambda = 4$, where solid lines correspond to a fattening droplet and dashed lines to a thinning droplet. Our numerical results reveal that for sufficiently small values of the volume (say $V \lesssim 37$) there is a clear distinct hysteretic behavior and the droplet follows different paths as the volume increases or decreases. However, for sufficiently large values of the volume ($V \gtrsim 37$), the droplet seems to settle into a more regular motion in which it remains at the same position independently of the volume, i.e., the droplet shift settles to a fixed value at large volumes. For this range of volumes, the only difference between increasing and decreasing the volume is observed at around $V \approx 43$ where the droplet quickly shifts back and forth giving rise to a small fluctuation. Figures 9c and 9e show the evolution of the half-width and contact angle, respectively, where we can see a similar hysteretic behaviour as the volume increases/decreases up to volumes $V \approx 43$, above which the droplet seems to settle to a regular behaviour—note that the small fluctuations observed in Figure 9a at
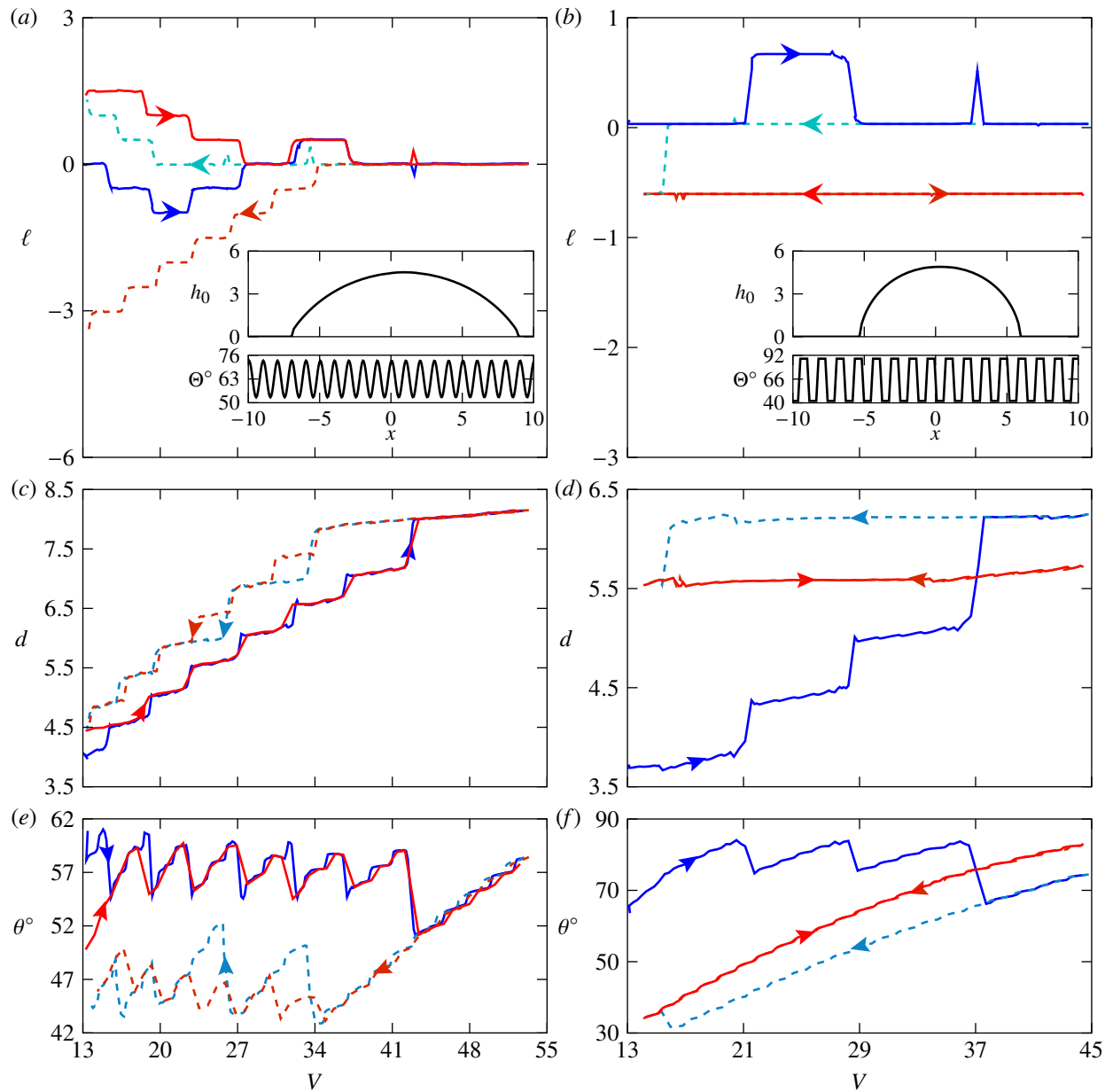
17

Figure 9: Computations of the droplet shift ℓ, half-width d, and contact angle θ during two cycles of increasing/decreasing the volume for two different types of chemical heterogeneities. Blue solid lines correspond to increasing volume and red dashed lines correspond to decreasing volume. (a,c,e) Sinusoidal heterogeneity given by eq 1 with $\Lambda = d_0/\lambda = 4$. (b,d,f) Stripped heterogeneity given by eq 2 with $\Lambda = 4$ which is alternating between hydrophilic patches with $\Theta = 45°$ and hydrophobic patches with $\Theta = 92°$. Inset panels in (a,b) show representative droplet shapes at a given time. In all panels, arrows indicate the direction of time.

$V \approx 43$ correspond, in fact, to a relatively large change on both the half-width and contact angle.
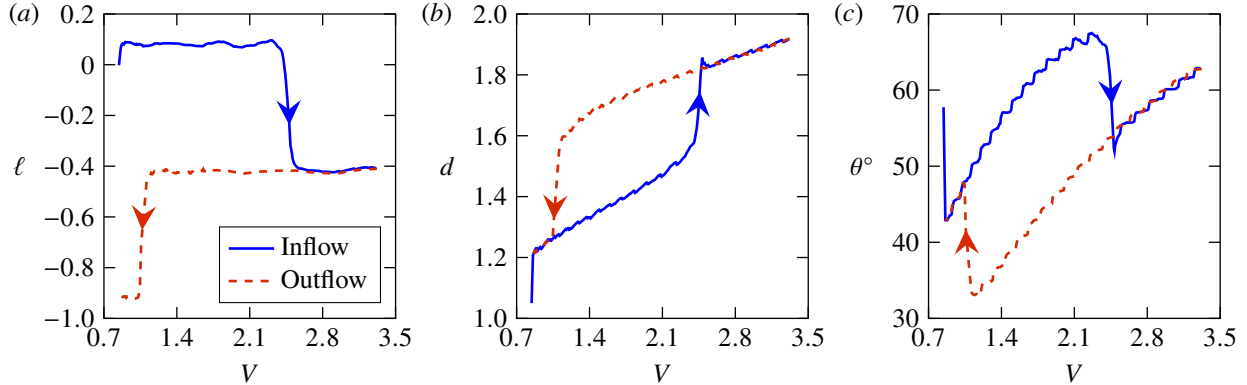
18

Figure 10: Computations of the different quantities characterizing the droplet dynamics as the volume is increased (blue solid lines) and decreased (red dashed lines) with a chemical heterogeneity given by eq 3 with $\sigma_2 = 5$, $\epsilon = 0.1$, and $\Lambda = d_0/\lambda = 1$. (a) Shift ℓ, (b) droplet half-width d, and (c) one of the contact angles θ. In all panels, arrows indicate the direction of time.

We have also considered a striped chemical heterogeneity which contains both hydrophilic and hydrophobic patches. The numerical results with $\Lambda = 4$ are presented in Figure 9b, where we can see that this type of chemical pattern tends to reduce hysteresis. We also observe that on the second cycle of increasing/decreasing the volume, the droplet stays pinned on the same location with the half-width remaining nearly constant and the contact angle increasing or decreasing with the volume.

Figure 10 shows the numerical results obtained with the multiscale variation given by eq 3. We can observe similar behavior in terms of stick-slip motion and hysteresis as for the pure sinusoidal chemical variation case, although now we also see variations occuring at shorter timescales precisely due to the multiscale character of the heterogeneities.

Analytical interpretation

The emergence of hysteresis is usually associated with the presence of stable and unstable states in the system. As we have shown in Figure 3, the stability of the equilibrium states depends on the volume of the droplet. Therefore, a way to characterize the emergence of such dynamic behavior is to compute the full bifurcation diagram as the volume changes. We
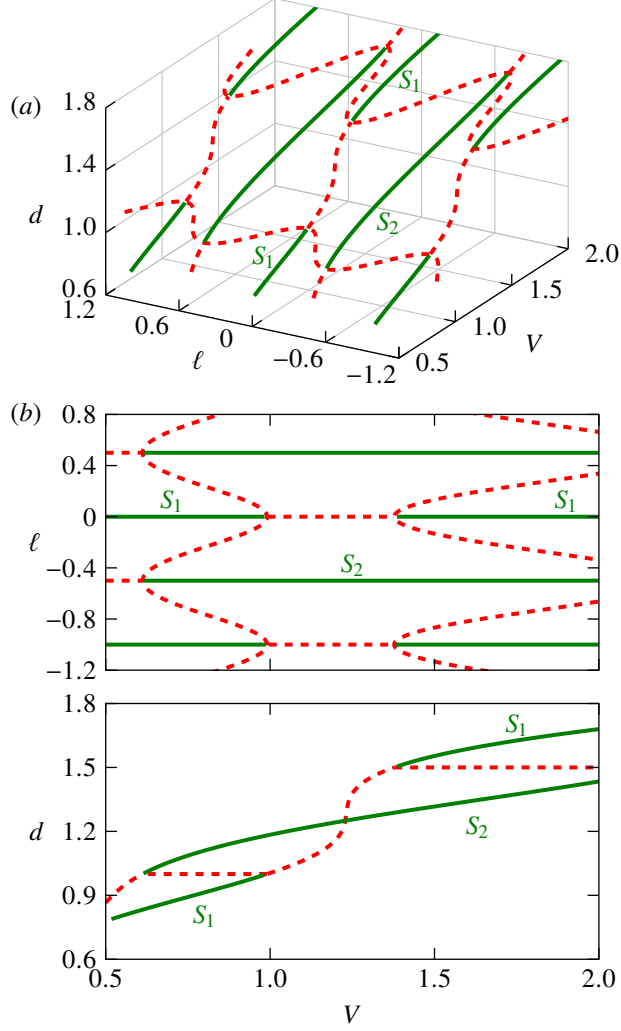
19

Figure 11: (a) Full 3D bifurcation diagram of the shift ℓ and droplet half-width d as the volume V of the droplet is increased. Red dashed and green solid lines denote saddle points and stable nodes, respectively. Panel (b) shows the corresponding 2D projections onto the (V, ℓ) (top) and (V, d) (bottom) planes, respectively. The labels S_1 and S_2 are used for reference across the different panels. The substrate chemical variation is given by eq 1 with $\theta_0 = 58°$, $\lambda = 1$, and $\sigma = 10$.

note, however, that since we have two independent variables, ℓ and d (changing d does not change ℓ and vice versa, while changing e.g. d will change θ) and one bifurcation parameter, V (changing V will change both d and ℓ), a co-dimension one phenomenon, the bifurcation diagram needs to be represented in a 3D graph. Figure 11 depicts the full bifurcation diagram for the sinusoidal case, including 2D projections to the (V, ℓ) plane and (V, d) plane.

Figure 11a reveals a complicated 3D bifurcation structure which is periodic along the

shift ℓ. It also reveals that the stability of the different equilibrium points changes as the volume is increased. This can be easily seen from the 2D projection onto the (V, ℓ) plane (top panel of Figure 11b). For small volumes ($V \approx 0.5$), there are two distinct equilibrium points, one of them being stable (denoted as S_1) while the other one is a saddle node. As the volume increases these points undergo a pitchfork bifurcation (in particular the stable node follows a subcritical pitchfork bifurcation while the saddle point follows an inverted supercritical pitchfork bifurcation) and so the stable node becomes a saddle, and the saddle becomes a stable node. At higher volumes, another set of pitchfork bifurcations takes place and the stability of both nodes is switched over again. Similarly, such a stability change induced by the volume is also observed in the bottom panel of Figure 11b, where the 3D bifurcation diagram is projected onto the (V, d) plane. It is noteworthy that a similar 2D diagram was reported in Ref. 32 although no information about the stability nor a complete picture of the bifurcation diagram, as it is provided here, was given. Moreover, as already emphasized in the introduction, Ref. 32 was restricted to equilibrium considerations only, since the volume was not changed dynamically as in our study; instead it was considered as a varying parameter in an equation governing droplet equilibrium. It should be noted that for even larger droplets (or equivalently smaller wave number λ in the periodic pattern given by eq 1) the bifurcation diagram exhibits additional complexities. Figure 12 shows the 2D projections of the bifurcation diagrams extended to larger volumes, where we can see the emergence of multiple equilibrium points found for the same shift ℓ. This is reflected as S-shape branches which appear at the (V, d) plane and which give rise to new unstable states.

An important point to remark is that the emergence of the stick-slip motion and hysteresis observed in the computational results presented in the previous section are caused by two factors, namely (a) the stability of the equilibrium points is affected by the droplet volume and, (b) the pitchfork bifurcations occurring at different branches along the shift do not take place at the same value of the volume. Indeed, Figure 13 shows a direct comparison of the
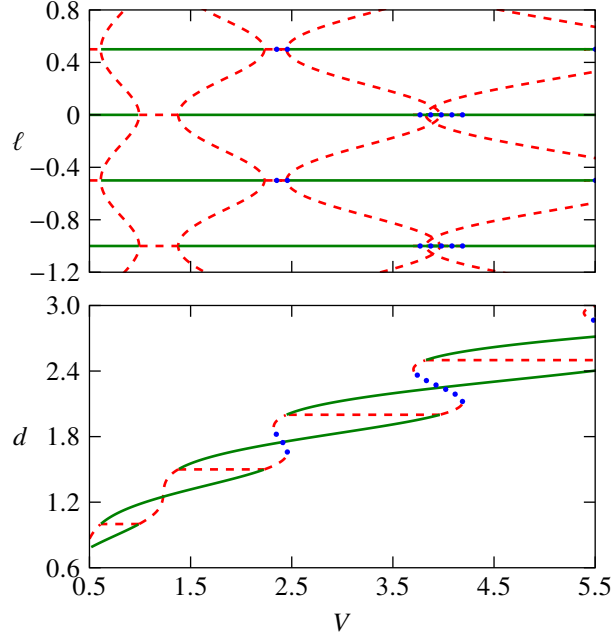
Figure 12: 2D projections of the bifurcation diagram extended to larger volumes. Red dashed, green solid, and blue dotted lines denote saddle nodes, stable nodes, and unstable nodes, respectively.

numerical dynamic simulation being plotted on top of the bifurcation diagrams where we can see a remarkable consistency between theory and numerical results. The top panel of Figure 13 shows the (V, ℓ) diagram where we observe that as the volume is increased the droplet follows a stable branch until there is a pitchfork bifurcation after which the droplet shifts to one of the two nearby stable branches. As the volume keeps on increasing, the droplet remains at this position until a second bifurcation occurs forcing the droplet to shift again to a nearby stable branch. At this point we started emptying by reverting to an outflow BC but the latter branch of equilibrium points remains stable as the volume is being decreased, allowing hence the droplet to remain at this position until another bifurcation occurs forcing the droplet to move again to another position. The bottom panel of Figure 13 shows the (V, d) diagram where we also observe the droplet is following a skeleton path composed of stable branches as the volume is increased and decreased. We note, however, that there is some disagreement between the numerical results and the analytically computed branches, particularly during outflow conditions, something which is in accordance to the fact that the
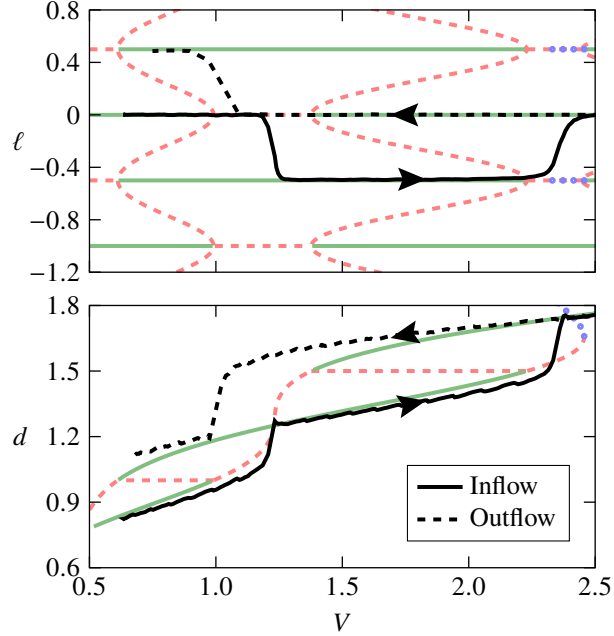
Figure 13: Comparison between the analytically obtained bifurcation diagram projected onto the (V, ℓ) (top) and (V, d) (bottom) planes and the time-dependent numerical results obtained by means of our diffuse interface formulation (solid line for inflow BC and dashed line for outflow BC). The substrate chemical variation is given by eq 1 with $\Lambda = 0.8$. Faint red dashed and green solid lines denote saddle points and stable nodes, respectively. In all panels, arrows indicate the direction of time.

droplet reamains on the $\ell = 0$ location long after the solution becomes unstable (cf. Figure 13, top panel).

A final remark from the complex bifurcation diagrams observed for the case of larger volumes (cf. Figure 12): we expect that for sufficiently large droplets the different sets of bifurcations will start to overlap with each other and the rate at which the stability of the solutions changes will be much faster than the growth rate of the volume droplet. At this point, the droplet may settle into a periodic motion where the effect of the chemical heterogeneities becomes irrelevant, as it was observed in the numerical computations presented in Figure 9.

Conclusions

We have scrutinized the equilibria and dynamics of a droplet on a chemically modified substrate. We have presented computational evidence that chemical heterogeneities play a crucial role on both the droplet equilibria and filling-emptying dynamics. Our computational framework is based on a diffuse-interface formulation together with an inflow-outflow BC (which we impose as an additional condition for the chemical potential), thus allowing for fluid to be pumped in and out of the droplet. Our model is expected to be valid in a regime of slow dynamics which is dominated by diffusion. It is also important to remark that in our study the droplet never detaches from the pore.

By imposing a simple periodic variation in the chemical properties of the substrate, we demonstrated that the motion of the droplet is characterized by very rich dynamic phenomena including hysteresis and a stick-slip motion of the contact points as the volume is varied. In particular, all the quantities which characterize the droplet, namely its shift, droplet half-width, and contact angle, undergo a hysteresis loop as the volume varies, indicating that the droplet follows different paths depending on whether the volume increases or decreases in time. In addition, our results demonstrate that such complex behavior becomes more prominent as the wavelength of the periodic chemical variation is decreased.

By analyzing in detail the equilibrium properties of the system, we have constructed the full bifurcation diagram depending on ℓ, d, and V. Since there are two independent parameters describing the position and shape of the droplet, namely its shift and droplet half-width, and one control parameter, the volume, the bifurcation diagram needs to be represented as a 3D graph which is characterized by a complex behavior where the equilibrium points change stability as the volume is increased. By looking in particular at an appropriate 2D projection of the full bifurcation diagram, we have been able to unravel a series of subcritical pitchfork bifurcations undergone by the droplet as its volume is increased, which in turn gives rise to stick-slip motion and hysteresis behavior. Our computational results are in excellent agreement with theoretical predictions obtained from the total interfacial energy

of the system.

Finally, it is important to note that even though we have considered a system where the volume of the droplet is modified by imposing an inflow-outflow BC, the results presented here are expected to be observed in other problems where droplets have a time-dependent volume variation, such evaporative systems.[20,49] Moreover, there is a number of interesting questions motivated by this study. For example, the problem droplets with a dynamic volume variation over not only periodic substrates but also more complex geometries, e.g. considering a chemical and/or topographical disorder. And quantifying hysteresis in terms of the strength of the disorder, either quenched as is the case here, or temporal, is one of the general basic questions in physics. Furthermore, geometries with multiscale effects, such as membranes or rough-fractal surfaces, are also of great importance in many different applications and understanding their interplay with an externally time-dependent control parameter, like the time-dependent volume imposed here, is an open question that still eludes us. We shall address these and related issues in future studies.

Acknowledgement

References

(1) Shanahan, M. E. R. Simple Theory of "Stick-Slip" Wetting Hysteresis. *Langmuir* **1995**, *11*, 1041–1043.

(2) Kusumaatmaja, H.; Yeomans, J. M. Modeling Contact Angle Hysteresis on Chemically Patterned and Superhydrophobic Surfaces. *Langmuir* **2007**, *23*, 6019–6032.

(3) Maheshwari, S.; Zhang, L.; Zhu, Y.; Chang, H.-C. Coupling Between Precipitation and Contact-Line Dynamics: Multiring Stains and Stick-Slip Motion. *Phys. Rev. Lett.* **2008**, *100*, 044503.

(4) Moffat, J. R.; Sefiane, K.; Shanahan, M. E. R. Effect of TiO_2 Nanoparticles on Contact Line Stick-Slip Behavior of Volatile Drops. *J. Phys. Chem. B* **2009**, *113*, 8860–8866.

(5) Savva, N.; Kalliadasis, S.; Pavliotis, G. A. Two-Dimensional Droplet Spreading over Random Topographical Substrates. *Phys. Rev. Lett.* **2010**, *104*, 084501.

(6) Savva, N.; Pavliotis, G. A.; Kalliadasis, S. Contact lines over random topographical substrates. Part 2. Dynamics. *J. Fluid Mech.* **2011**, *672*, 384–410.

(7) Orejon, D.; Sefiane, K.; Shanahan, M. E. R. Stick-Slip of Evaporating Droplets: Substrate Hydrophobicity and Nanoparticle Concentration. *Langmuir* **2011**, *27*, 12834–12843.

(8) Wylock, C.; Pradas, M.; Haut, B.; Colinet, P.; Kalliadasis, S. Disorder-induced hysteresis and nonlocality of contact line motion in chemically heterogeneous microchannels. *Phys. Fluids* **2012**, *24*, 032108.

(9) Savva, N.; Kalliadasis, S. Droplet motion on inclined heterogeneous substrates. *J. Fluid Mech.* **2013**, *725*, 462–491.

(10) Varagnolo, S.; Ferraro, D.; Fantinel, P.; Pierno, M.; Mistura, G.; Amati, G.; Biferale, L.; Sbragaglia, M. Stick-Slip Sliding of Water Drops on Chemically Heterogeneous Surfaces. *Phys. Rev. Lett. 111*, 066101.

(11) Kajiya, T.; Daerr, A.; Narita, T.; Royon, L.; Lequeux, F.; Limat, L. Advancing liquid

contact line on visco-elastic gel substrates: stick-slip *vs.* continuous motions. *Soft Matter* **2013**, *9*, 454–461.

(12) Aydemir, C. Time-Dependent Behavior of a Sessile Water Droplet on Various Papers. *Int. J. Polym. Mater.* **2010**, *59*, 387–397.

(13) Espin, L.; Kumar, S. Droplet spreading and absorption on rough, permeable substrates. *J. Fluid Mech.* **2015**, *784*, 465–486.

(14) Trabold, T. A. Minichannels in polymer electrolyte membrane fuel cells. *Heat Transfer Eng.* **2005**, *26*, 3–12.

(15) Colosqui, C.; Cheah, M.; Kevrekidis, I.; Bezinger, J. Droplet and slug formation in polymer electrolyte membrane fuel cell flow channels: The role of interfacial forces. *J. Power Sources* **2011**, *196*, 10057–10068.

(16) Gauthier, E.; Hellstern, T.; Kevrekidis, I.; Bezinger, J. Drop Detachment and Motion on Fuel Cell Electrode Materials. *ACS Appl. Mater. Interfaces* **2012**, *4*, 761–771.

(17) Cheah, M.; Kevrekidis, I.; Benzinger, J. Water Slug Formation and Motion in Gas Flow Channels: The Effects of Geometry, Surface Wettability, And Gravity. *Langmuir* **2013**, *29*, 9918–9934.

(18) Anderson, D. M.; Wilson, S. H. The spreading of volatile liquid droplets on heated surfaces. *Phys. Fluids* **1995**, *7*, 248.

(19) Gelderblom, H.; Marín, A. G.; Nair, H.; van Houselt, A.; Lefferts, L.; Snoeijer, J. H.; Lohse, D. How water droplets evaporate on a superhydrophobic substrate. *Phys. Rev. E* **2011**, *83*, 026306.

(20) Ledesma-Aguilar, R.; Vella, D.; Yeomans, J. M. Lattice-Boltzmann simulations of droplet evaporation. *Soft Matter* **2014**, *10*, 8267–8275.

(21) Stauber, J. M.; Wilson, S. K.; Duffy, B. R.; Sefiane, K. On the lifetimes of evaporating droplets. *J. Fluid Mech.* **2014**, *744*, R2 (12 pages).

(22) Stauber, J. M.; Wilson, S. K.; Duffy, B. R.; Sefiane, K. On the lifetimes of evaporating droplets with related initial and receding contact angles. *Phys. Fluids* **2015**, *27*, 122101.

(23) Sáenz, P. J.; Sefiane, K.; Kim, J.; Matar, O. K.; Valluri, P. Evaporation of sessile drops: a three-dimensional approach. *J. Fluid Mech.* **2015**, *772*, 705–739.

(24) Oliver, J. M.; Whiteley, J. P.; Saxton, M. A.; Vella, D.; Zubkov, V. S.; King, J. R. On contact-line dynamics with mass transfer. *Eur. J. Appl. Math.,* **2015**, 1–49, Available on CJO 2015 doi:10.1017/S095679251500036.

(25) Ambravaneswaran, B.; Phillips, S. D.; Basaran, O. A. Theoretical Analysis of a Dripping Faucet. *Phys. Rev. Lett.* **2000**, *85*, 5332–5335.

(26) Ambravaneswaran, B.; Subramani, H. J.; Phillips, S. D.; Basaran, O. A. Dripping-Jetting Transitions in a Dripping Faucet. *Phys. Rev. Lett.* **2004**, *93*, 034501.

(27) Collister, C.; Mattey, D. Controls on water drop volume at speleothem drip sites: An experimental study. *J. Hydrol.* **2009**, *358*, 259–267.

(28) Kamusewitz, H.; Possart, W. The static contact angle hysteresis obtained by different experiments for the system PTFE/water. *Int. J. Adhesion and Adhesives* **1985**, *5*, 211–215.

(29) Drelich, J.; Miller, J. D.; Good, R. J. The Effect of Drop (Bubble) Size on Advancing and Receding Contact Angles for Heterogeneous and Rough Solid Surfaces as Observed with Sessile-Drop and Captive-Bubble Techniques. *J. Colloid Interface Sci.* **1996**, *179*, 37–50.

(30) Hennig, A.; Eichhorn, K. J.; Staudinger, U.; Sahre, K.; Rogalli, M.; Stamm, M.; Neumann, A. W.; Grundke, K. Contact Angle Hysteresis: Study by Dynamic Cycling Con-

tact Angle Measurements and Variable Angle Spectroscopic Ellipsometry on Polyimide. *Langmuir* **2004**, *20*, 6685–6691.

(31) Marmur, A. Contact Angle Hysteresis on Heterogeneous Smooth Surfaces. *J. Colloid Interface Sci.* **1994**, *168*, 40–46.

(32) Brandon, S.; Marmur, A. Simulation of Contact Angle Hysteresis on Chemically Heterogeneous Substrates. *J. Colloid Interface Sci.* **1996**, *183*, 351–355.

(33) Extrand, C. W. A Thermodynamic Model for Contact Angle Hysteresis. *J. Colloid Interface Sci.* **1998**, *207*, 11–19.

(34) Brandon, S.; Haimovich, N.; Yeger, E.; Marmur, A. Partial Wetting of Chemically Patterned Surfaces: The Effect of Drop Size. *J. Colloid Interface Sci.* **2003**, *263*, 237–243.

(35) Vellingiri, R.; Savva, N.; Kalliadasis, S. Droplet spreading on chemically heterogeneous substrates. *Phys. Rev. E* **2011**, *84*, 036305.

(36) Anderson, D.; McFadden, G.; Wheeler, A. Diffuse-interface methods in fluid mechanics. *Annu. Rev. Fluid Mech.* **1998**, *30*, 139–165.

(37) Khatavkar, V. V.; Anderson, P. D.; Meijer, H. E. H. Capillary spreading of a droplet in the partially wetting regime using a diffuse-interface model. *J. Fluid Mech.* **2007**, *572*, 367–387.

(38) Yue, P.; Zhou, C.; Feng, J. Sharp-interface limit of the Cahn-Hilliard model for moving contact lines. *J. Fluid Mech.* **2010**, *645*, 279–294.

(39) Sibley, D.; Nold, A.; Kalliadasis, S. Unifying binary fluid diffuse-interface models in the sharp-interface limit. *J. Fluid Mech.* **2013**, *736*, 5–43.

(40) Briant, A.; Papatzacos, P.; Yeomans, J. M. Lattice Boltzamn simulations of contact line motion in a liquid-gas system. *Phil. Trans. Roy. Soc. Lond. A* **2002**, *360*, 485–495.

(41) Cahn, J. W. Critical point wetting. *J. Chem. Phys.* **1977**, *66*, 3667–3672.

(42) de Gennes, P. G. Wetting: statics and dynamics. *Rev. Mod. Phys.* **1985**, *57*, 827–863.

(43) Seppecher, P. Moving contact lines in the Cahn-Hilliard theory. *Int. J. Eng. Sci.* **1996**, *34*, 977–992.

(44) Jacqmin, D. Contact-line dynamics of a diffuse fluid interface. *J. Fluid Mech.* **2000**, *402*, 57–88.

(45) Sibley, D.; Nold, A.; Savva, N.; Kalliadasis, S. The contact line behaviour of solid-liquid-gas diffuse-interface models. *Phys. Fluids* **2013**, *25*, 092111.

(46) Huang, J. J.; Shu, C.; Chew, Y. T. Lattice Boltzmann study of droplet motion inside a grooved channel. *Phys. Fluids* **2009**, *21*, 022103.

(47) Papatzacos, P. Macroscopic two-phase flow in porous media assuming the diffuse-interface model at pore level. *Transport Porous Med.* **2002**, *49*, 139–174.

(48) Hohenberg, P.; Halperin, B. Theory of dynamic critical phenomena. *Rev. Mod. Phys.* **1977**, *49*, 435–479.

(49) Rednikov, A.; Colinet, P. Singularity-free description of moving contact lines for volatile liquids. *Phys. Rev. E* **2013**, *87*, 010401(R).

Graphical TOC Entry
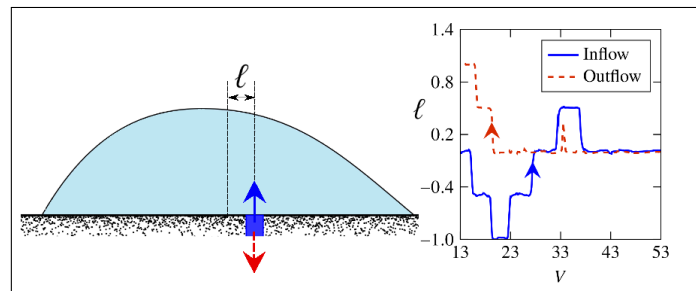
Liquid is pumped in or out through a pore (blue patch) into a droplet on a chemically heterogeneous planar substrate. Right panel shows the droplet shift ℓ as its volume increases (solid blue line) or decreases (dashed red line). Arrows indicate direction of time.